Fuel Processing Technology 184 (2019) 45–56

Contents lists available at ScienceDirect

Fuel Processing Technology

journal homepage: www.elsevier.com/locate/fuproc

Research article

Bio-additive fuels from glycerol acetalization over metals-containing vanadium oxide nanotubes (MeVO$_x$-NT in which, Me = Ni, Co, or Pt)

Andre Luis G. Pinheiro[a], José Vitor C. do Carmo[a], Davi C. Carvalho[a], Alcineia C. Oliveira[a,*], Enrique Rodríguez-Castellón[b], Samuel Tehuacanero-Cuapa[c], Larissa Otubo[d], Rossano Lang[e]

[a] Universidade Federal do Ceará, Campus do Pici-Bloco 940, Departamento de Química Analítica e Físico-Química, Fortaleza, Ceará, Brazil
[b] Universidad de Málaga, Departamento de Química Inorgánica, Facultad de Ciencias, 29071 Spain
[c] Instituto de Física, UNAM, Circuito de la Investigación s/n, Ciudad Universitaria, 04510 Coyoacán, D.F., Mexico
[d] Centro de Ciência e Tecnologia de Materiais - CCTM, Instituto de Pesquisas Energéticas e Nucleares - IPEN, 05508-000 São Paulo, São Paulo, Brazil
[e] Instituto de Ciência e Tecnologia - ICT, Universidade Federal de São Paulo UNIFESP, 12231-280, São José dos Campos, São Paulo, Brazil

ARTICLE INFO

Keywords:
Vanadium oxides
Nanotubes
Glycerol
Acetalization
Biofuels

ABSTRACT

The biodiesel production has led to a drastic surplus of glycerol and catalytic conversion of glycerol into value-added products is of great industrial importance. Thus, the acetalization of glycerol with ketone or aldehydes allows the glycerol transformation into bio–additive fuels. In this work, metals-containing vanadium oxides nanotubes (MeVO$_x$ NT in which, Me = Co, Pt or Ni) have been synthesized with additional internal porosity and tested in the acetalization of glycerol with acetone (AG) for valuable biofuels production. The catalysts showed remarkable performances in the AG reaction. Furthermore, by variation of the composition, catalyst loading and temperature and using distinct substrates (butyraldehyde, furfuraldehyde and benzaldehyde), NiVO$_x$NT is active, being very selective to solketal and reciclable for 4 times in the AG reaction. On the contrary, pure VO$_x$ NT easily deactivated due to the structure agent removal during the reaction, which promote the collapse of the tubular structure. The CoVO$_x$NT and PtVO$_x$NT catalysts did not exhibit such a stable structure and easily deactivated in the reaction due to leaching of the metals oxides during the AG.

1. Introduction

Recently, the interest in glycerol as a renewable feedstock for biofuels and chemicals production has become increasingly important [1]. Glycerol is a promising biomass platform molecule having several applications in many fields, for instance, as pharmaceutical medicine intermediate, additive for biodegradable compounds as well as in food and resins production [2,3]. Although all these sustainable alternatives, the requirement of using pure glycerol is imperatively needed for its applications. Therefore, to further expand glycerol uses, it is necessary to approach the drawback of purifying the trialcohol, owing to the low energy-efficient and cost-effective purification process [1–4].

To address this challenge, the catalytic transformations of glycerol offer the advantage of the direct use of the trialcohol for selective value-added chemical production. These strategies consist of many different routes such as acetalization, dehydration, oxidations, reforming, among others routes [5–9]. The glycerol acetalization, in particular, that is a condensation reaction, uses glycerol and carbonyl compounds, e.g., aldehydes or ketones targeting cyclic glycerol acetal/ketal molecules. For instance, the scheme 1 shows a reversible reaction between glycerol and acetone producing (1,3-dioxolan-4-yl) methanol (solketal), 1,3-dioxan-5-ol (acetal) and water, where R_1 and R_2 are the CH_3 radical [3,9], as shown in Fig. 1. The readily available 5-membered solketal and 6-membered acetal cyclic compounds are obtained from low-cost glycerol. Moreover, they have been widely used in industry, as fuel additives to improve low-temperature flow properties, solvents, surfactants, humectants and binders [3,5–12].

The reaction has been traditionally carried out using supported and unsupported catalysts. Zeolites, acidic resins, zeotypes, supported heteropolyacids, mixed oxides, sulfonate mesoporous materials, activated carbons, rare-earth triflates, nanoparticles supported on active carbon or multi-walled carbon nanotubes and metal oxides nanotubes are frequently used in the reaction [9–15]. Some of these catalysts have appreciable activity in the reaction when substrates like acetone, formaldehyde, butyraldehyde, methyl levulinate are used in mild conditions [11–15]. Nevertheless, despite the great potential of the aforesaid catalysts, the production of some of them is costly, being too expensive to be applied in the large-scale production.

* Corresponding author.
E-mail address: alcineia@ufc.br (A.C. Oliveira).

https://doi.org/10.1016/j.fuproc.2018.11.008
Received 16 July 2018; Received in revised form 10 October 2018; Accepted 8 November 2018
Available online 20 November 2018
0378-3820/

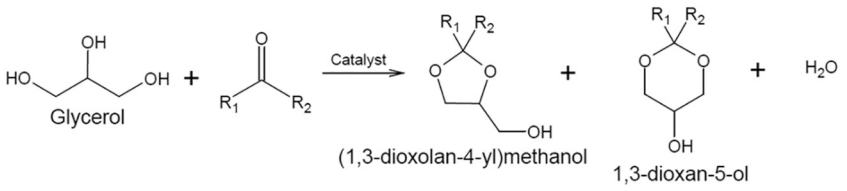

Fig. 1. Schematic representation of the acetalization of glycerol with acetone.

Most recently, cheap metal oxide catalysts have been applied, but they are not sufficiently stable for the reaction [1,16,17]. Particularly, the combination of supported Sn, W, Nb, Ni, Cu, Ti, Co, Mo and V oxides as acid-base and redox catalysts have been proven to be efficient for glycerol acetalization with acetone reaction [10–15]. Besides, solid acid catalysts have been tested successfully in the glycerol acetalization reaction [2–4]. However, the acid catalysts may suffer from the leaching of the active acid sites and exhibit poor hydrothermal stability [1,12]. Although the above solids are extremely promising, supported metal nanotube oxide catalysts (MeTNT in which, Me = Ni, Co or Pt) may be more suitable for the practical acetalization of glycerol because of the availability of their active sites, product distribution, selectivity and low cost [12]. In addition, the tubular morphology plays an important role in obtaining active sites either confined or dispersed on the nanotube support.

In this sense, the excellent catalytic performance of the metal-containing titanium oxide nanotubes e.g., Ni, Pt or Co are essentially due to the molecules confinement effects, although their shortcomings, for example, their low stability against leaching is intriguing [12].This motivates us to search for new catalytic systems with tubular morphology and variability in their Lewis acid metal sites to the reaction. To the best of our knowledge, the $MeVO_x$-NT in which, Me = Ni, Co or Pt have never been used in the reaction. The $MeVO_x$ NT could play a key role towards the selective formation of the solketal product, high thermal stability and the water–tolerant property to avoid weakening the acidic sites.

Herein, vanadate oxide nanotubes (VO_x-NTs) containing metals ($MeVO_x$-NT; Me = Ni, Co, and Pt) were synthesized and used as catalysts for the glycerol acetalization with acetone (AG). Furthermore, active species of vanadium oxide nanotubes, as well as their structural effects, have been discussed in detail by a combination of experimental and characterizations data. One observed that the dispersion of Ni on the VO_x-NTs significantly improves the conversion of glycerol and the selectivity to the cyclic acetals, when exploited in several reaction conditions. On the other hand, the $CoVO_x$-NT and $PtVO_x$-NT catalysts easily deactivated during the AG reaction.

2. Experimental

2.1. Vanadium oxides nanotubes preparation

Pure and metal-containing vanadate nanotubes, i.e., $MeVO_x$-NTs (Me = Ni, Co, and Pt) were synthesized following a previously reported procedure with some modifications [18]. Briefly, 1.5 g of vanadium pentoxide (Aldrich) were dispersed in a mixture of 1.5 g of dodecylammonium chloride (Aldrich) and 14 mL of ethanol (Aldrich), under stirring at room temperature for 2 h. Afterward, the resulting suspension was redispersed in distilled water with continuous stirring for 48 h. The mixture was then, placed in a Teflon-lined stainless steel autoclave under auto-generated pressure and heated at 165 °C for 4 days. Finally, the remaining wet solid was separated by centrifugation, washed, dried at 30 °C overnight and subsequently vacuum dried at 50 °C for 10 h. The as-synthesized vanadium oxide nanotubes powder was denoted as VO_x-NT.

The ion exchange process was performed by using 100 mg of VO_x-NT in the presence of 100 mL of cobalt(II) nitrate ($Co(NO_3)_2{\cdot}6H_2O$) or nickel(II) nitrate ($Ni(NO_3)_2{\cdot}6H_2O$) solutions (both from Vetec), under stirring for 24 h. The obtained solids were washed with ethanol for several times to remove the nitrate precursors, centrifuged and dried in ambient air at 80 °C for 24 h. The solids possessing a concentration of 1 wt% of Ni and Co were labeled as $NiVO_x$-NT and $CoVO_x$-NT, respectively. The wet impregnation method was applied to incorporate Pt to the VO_x-NT. In a typical procedure, about 1 mL of the hexachloroplatinic acid solution (H_2PtCl_6, Aldrich) per gram of VO_x-NT was added to a rotary evaporator under stirring at room temperature for 2 h. The solid was subsequently recovered, washed thoroughly with ethanol to remove the chlorined precursor and dried at 80 °C for 24 h to obtain the $PtVO_x$-NT solid with 1 wt% of Pt.

2.2. Catalysts characterization

X-ray diffraction (XRD) measurements were carried out at room temperature by using a Bruker D8 Advance diffractometer with Cu-Kα1 (1.5406 Å) radiation (40 kV and 40 mA) at a scanning step of 0.02° with accounting time of 1 s at every step, over the 2θ range of 10°–65°. Moreover, low angle measurements between 2° and 10° were also performed. The patterns were compared to those of the Joint Committee on Powder Diffraction Standards (JCPDS) data.

Micro-Raman scattering spectra were acquired on a microscope alpha 300 from Witec using the confocal microscopy method. The spectra were excited at 532 nm and collected with 5 data acquisitions per 120 s. The measurements were obtained in the wavenumber range between 100 and 2000 cm^{-1} at room temperature by using an average laser power of 5 mW on the sample surface. A silicon substrate was used as a reference at 521 cm^{-1}. The spectral resolution was about 2 cm^{-1}.

Fourier-transformed infrared spectroscopy (FTIR) measurements of the solids were performed on an FT-IR VERTEX 70 spectrophotometer from Brucker at ambient conditions using KBr discs. The spectra were recorded in the 400–4000 cm^{-1} range. The nominal resolution was about 2 cm^{-1}.

Transmission electron microscopy (TEM) images were obtained on an FEI Tecnai 20 G2 and JEOL JEM-2100 electron microscope; both operated at 200 kV. Previously, the samples were dispersed in ethanol in an ultrasonic bath for few minutes and subsequently, deposited on a perforated carbon foil supported by a copper grid.

Scanning electron microscopy (SEM) analyses were performed on a TESCAN VEGA XMU electron microscope equipped with an energy dispersive X-ray spectroscopy (EDS) system coupled from EDS Bruker QUANTAX. Prior to the analyses, the samples were prepared by dispersing the catalyst powder in an aluminum sample holder and sputtering the samples with gold.

Inductively coupled plasma optical emission spectroscopy (ICPOES) analyses were carried out on a Varian apparatus to determine the metal contents of the solids as well as the remaining solution after glycerol acetalization with acetone. Previous digestion of the solids with a mixture of nitric and hydrochloric acids at 90 °C was performed.

Surface area, size and volume of pore were measured by nitrogen adsorption-desorption isotherms at −196 °C in a Micromeritics ASAP 2420 apparatus. Previously, samples were degassed under vacuum at 90 °C for 24 h. The surfaces areas were determined through Brunauer-Emmett-Teller (BET) method whereas pore volumes were obtained from nitrogen adsorbed at a relative pressure of 0.998. The pore size distribution was determined using the Barrett-Joyner-Halenda (BJH) method from the desorption branch of the N_2 isotherms.

X-ray Photoelectron Spectra (XPS) were recorded on a physical electronics spectrometer (PHI Versa Probe II Scanning XPS Microprobe) with monochromatic X-ray Al-Kα radiation at 1486.6 eV as the excitation source (100 μm diameter of the X-ray highly focused beam, 100 W, 20 kV). High-resolution multi-region spectra were obtained at a given take-off angle of 45° by a concentric hemispherical analyzer operating in the constant pass energy mode at 23.5 eV. The spectrometer energy scale was calibrated using Cu $2p_{3/2}$, Ag $3d_{5/2}$, and Au $4f_{7/2}$ photoelectron lines at 932.7, 368.2 and 84.0 eV, respectively. PHI Smart Soft-VP 2.6.3.4 software package was used for the data analysis. A Shirley-type background was subtracted from the signals, and the recorded spectra were fitted using Gauss-Lorentz curves. The binding energies were referenced to the C 1s peak of adventitious carbon at 284.6 eV. The V 2*p* and C 1s spectra were first registered with a short irradiation time of 10 min to avoid vanadium photoreduction.

2.3. Catalytic experiments

Acetalization of glycerol with acetone (AG) was carried out under batch conditions in a Parr Instruments batch reactor, which was equipped with a mechanic stirrer and a thermocouple. The reaction started using an equimolar mixture of acetone and glycerol, being both reactants transferred into the batch reactor containing the prepared catalysts. For each experiment, 130 mg of the fresh catalyst was loaded into the reactor, corresponding to roughly 5% of the total reactor volume.

The resulting mixture was stirred at 50 °C to ensure completeness of the reaction. The samples were periodically withdrawn and analyzed using a Gas Cromatograph (G-8000 Intercrom GC) equipped with a capillary column and flame ionization detector (FID). 1-Dimethylformamide was used as internal standard.

All the products were confirmed by using a Gas Chromatograph coupled to Mass spectrometer (CG-MS) Shimadzu QP5050. The reaction temperature, catalyst mass and glycerol to acetone molar ratios were varied to optimize the reaction conditions. The catalytic runs were also carried out using other substrates than acetone such as furfuraldehyde (FUR), butyraldehyde (BUT) and benzaldehyde (BEN). The reaction conditions were at 50 °C, acetone to glycerol molar ratio of 1, using 130 mg of catalyst for 6 h of reaction.

Blank runs were performed for correction using no catalysts and glycerol conversion were less than 10%, depending on the temperature used.

The catalytic recyclability tests of the most active solids were also performed. Briefly, the catalyst was removed after reaction, being separated by filtration, washed with water, dried in vacuum at 80 °C for 6 h, and finally used for the next run without adding any fresh catalyst. Moreover, the glycerol conversion, acetal selectivities, and turnover frequency (TOF) were determined, according to the previous calculations [12].

3. Results and discussion

3.1. Morphological and structural aspects of the as-synthesized vanadium oxide nanotubes

3.1.1. SEM-EDS and TEM analyses

The morphology of the solids is demonstrated by SEM images. The VO_x-NTs has an open-ended multiwalled tubular structure (Fig. 2a) as reported in the literature [18–20]. The corresponding EDS spectrum indicates a homogenous distribution of V and O, with carbon from the structure directing an agent on the solid surface. The C, N and Cl elements come from the dodecylammonium chloride structuring agent included in the tubes.

$NiVO_x$-NT and $CoVO_x$-NT samples also depict a tubular morphology, which is indeed similar to that of VO_x-NT, as illustrated in Fig. 2b and c, respectively. These samples possess tangled nanotubes with an obvious presence of cobalt or nickel species on the surfaces, as shown by the EDS spectra. Further observation by TEM micrographs reveals that the Ni^{2+} and Co^{2+} species are not located on the outer surface but, mostly intercalated into the VO_x-NT layers.

Interestingly, $PtVO_x$-NT does not exhibit the hollow tubular morphology (Fig. 2d), evidencing that the impregnation of Pt species gives rise to an aggregation of the tubes by forming nanosheets. This is due to the stress of the tubes caused by mechanic agitation during the preparation of the solid. Besides, some Pt species are found on the solid surface, as indicated by the EDS analysis. The C, N and Cl elements arise from the hexachloroplatinic acid and dodecylammonium chloride reactants used during the synthesis.

The TEM images further confirm the tubular-shaped morphology of the as-synthesized VO_x-NTs nanotubes. The pristine VO_x-NT sample (Fig. 3a) has well-defined hollow interiors with an inner diameter varying from 30 to 44 nm and outer diameter in the 89–110 nm range. The tubes are formed by 13–16 layered walls and lengths of up to several microns that are consistent with the values reported in the literature for a similar synthesis [20–24]. Also, the tubes possess average interlayer distances of around 2.86 nm, in line with the XRD results which will be displayed and discussed further below.

After ion exchange process, no clear differences in terms of morphology are observed for $NiVO_x$-NT (Fig. 3b) and $CoVO_x$-NT (Fig. 3c). Accordingly, the outer diameter of VO_x-NT is about 110 nm and the ion exchange process has triggered the drop of diameters to 107 and 100 nm, respectively for $NiVO_x$-NT and $CoVO_x$-NT. A reasonable explanation for this is that the replacement of the docecylamonium cation for Ni^{2+} or Co^{2+} into the tubes shrinks the nanotubes to accommodate the metals in the structure and hence, giving the stability of the structure. In a good agreement, the metals nanoparticles are neither on the tube surface nor included in the tubes, as observed by the images. On the basis of published works, the amine surfactant molecules are readily exchanged with transition metal ions, while the tubular morphology is preserved [24,25]. In case of the $PtVO_x$-NT sample, Fig. 3d, the nanoparticles supposedly from Pt species (PtO_xCl, $Pt(OH)Cl_x$ and PtO_x) are observed either in the inner or outer surfaces of the solid. Indeed, the diameter of the tubes varies between 53 and 70 nm, suggesting somehow a collapse of the tubes due to the bulky Pt particles.

3.1.2. XRD results

Fig. 4a shows the low-angle XRD patterns of the as-synthesized VO_x-NTs. The pristine VO_x-NT catalyst exhibits a broad feature with the (001), (002) and (003) reflections corresponding to the well-ordered layered structure of monoclinic [21,22], in agreement with the TEM results. The findings state that the reflection appearing at $2\theta = 3.1°$ (001) is regarded as the two-dimensional vanadium lamellar structures with the VO_x within the layers [20]. In line with this, the interlayer value is about 2.86 nm, implying that the dodecylamine chains are mostly intercalated in the tubular region. The incorporation of the metals in the VO_x-NT structure shifts the (001) reflection to higher diffraction angles, with a consequent decrease of the interlayer distance from 2.86 nm to 1.25 nm and 1.09 nm, for $NiVO_x$-NT and $CoVO_x$-NT, respectively. Such a result suggests that the dodecylamine chain structure directing agent was replaced by Ni or Co. For $PtVO_x$-NT sample, the peak corresponding to the (001) reflection shifts to $2\theta = 4.3°$, which indicates shrinkage of the tubular structure to 2.06 nm. The fact is that some Pt nanoparticles may be entrapped in vanadate structure with a subsequent low degree of structural ordering of the solid.

It is clear that at higher diffraction angles (Fig. 4b), the intensity of the diffraction peaks is relatively weak, which may be related to their two-dimensional structure of VO_x layers in low ordering. As can be observed from the $NiVO_x$-NT and $CoVO_x$-NT diffractogram, the peak at $2\theta \approx 35°$ confirms the insertion of Ni^{2+} or Co^{2+} in the tubular structure showing the successful removal of organic dodecylamine within the vanadate layers. To support these achievements, cations with a similar

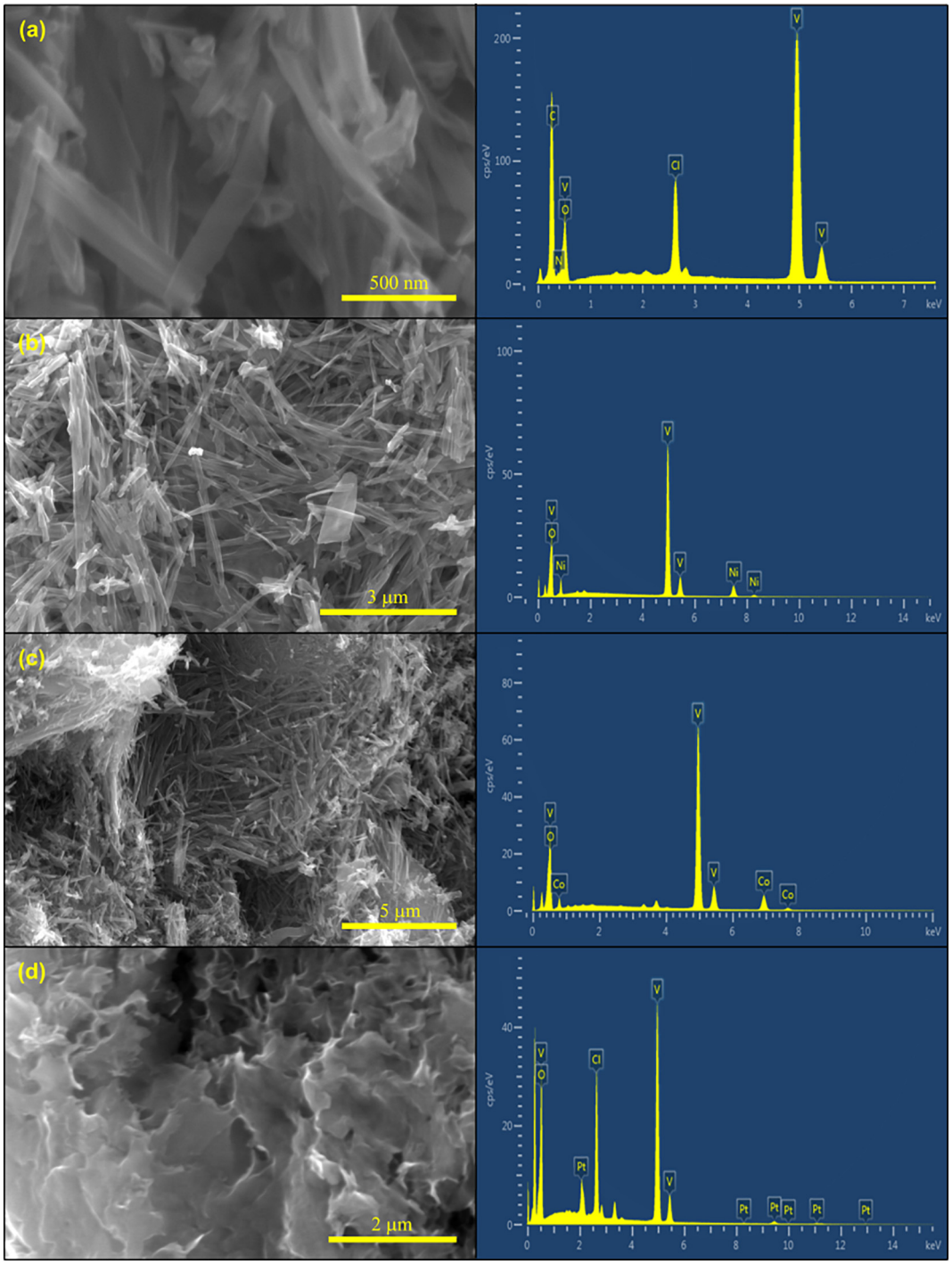

Fig. 2. SEM images and EDS spectra of the samples: (a) pure VO_x-NT, (b) $NiVO_x$-NT, (c) $CoVO_x$-NT and (d) $PtVO_x$-NT.

charge to radius ratios as Fe^{3+}, Co^{3+}, and Ni^{2+} are included into the space between VO_x nanotube layers, when they are successfully incorporated to the nanotubes by ion exchange [24–26]. Through the maintenance of peak positions assigned to (210), (310), (320) and (400) reflections, one can expect that the internal walls of the solids are not affected by the ion exchange process. Furthermore, the $PtVO_x$-NT diffractogram does not display any peak associated with Pt species, which indicate they may be either dispersed on surface or intercalated in the VO_x-NT layers as observed by TEM. This will be better discussed through the spectroscopic measurements. In summary, the reflections associated with Ni, Co or Pt oxide are not observed because of its low loading (less than 1.5%) and the particle sizes at nanometric scale.

3.1.3. Structural features of the solids by FTIR and micro-Raman

FTIR and micro-Raman spectroscopy measurements were performed in order to examine the vibrational structures of the as-synthesized vanadium oxide nanotubes. FTIR spectrum of the pure VO_x-NT sample reveals the characteristic broad absorption band at 3200–3700 cm^{-1} (Fig. 4c) from physisorbed water molecules. Especially, the stretching and bending vibrations from hydroxyl groups from water are seen respectively at ≈3440 and at ≈1615 cm^{-1} [23]. In addition, the absorption bands at ≈2850, 2920 and 2960 cm^{-1} are assigned to the ν(C—H) vibrations from the residue of dodecylammonium molecule, e.g., $C_{12}H_{25}NH_3^+$ [23]. Also, the δ(C—H) vibrations are observed at around 1460 cm^{-1}. The absorption bands located at 1500 and

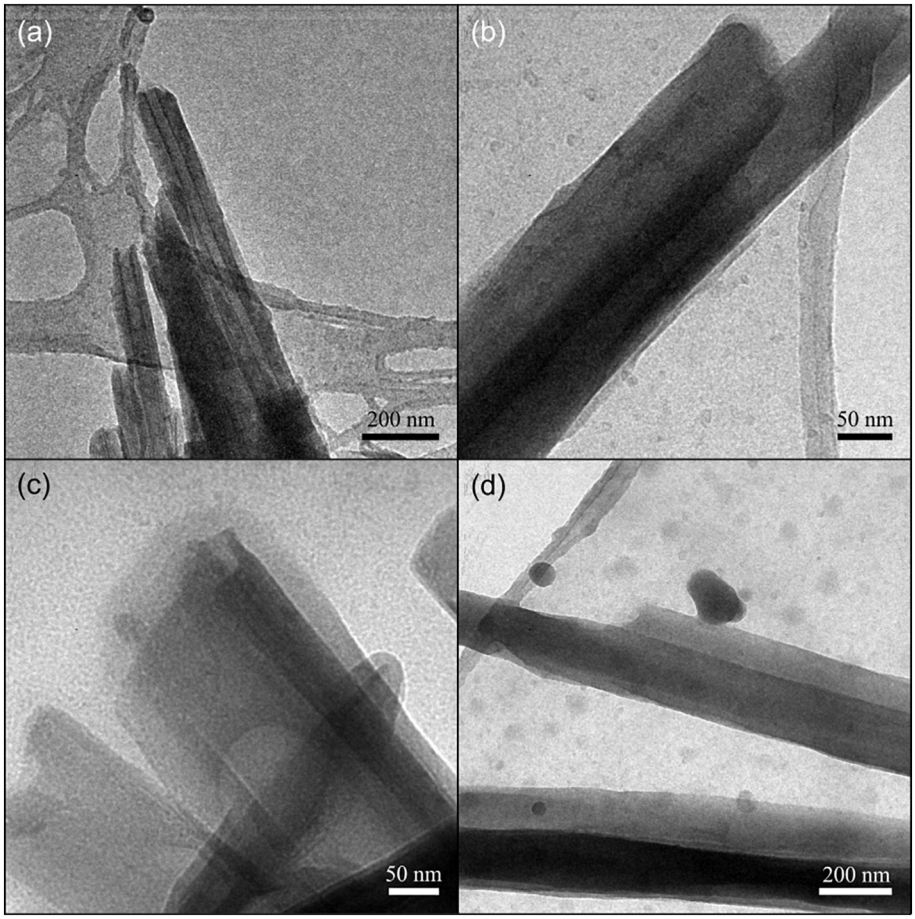

Fig. 3. TEM images of the solids: (a) pure VO_x-NT, (b) $NiVO_x$-NT, (c) $CoVO_x$-NT and (d) $PtVO_x$-NT.

1605 cm^{-1} correspond to the stretching of N—H bonds, respectively [24,25]. The bands at around 490, 575 and 640 cm^{-1} are assigned to the asymmetric stretching of the V—O—V vibrations. The absorption bands appearing at about 1000 cm^{-1} is assigned to ν(V═O) vibration [23,24]. Moreover, a band of low intensity at 930 cm^{-1} is due to the stretching V—O···H vibrations from vanadyl groups [24], in good agreement with the XRD, TEM and SEM results.

Incorporation of either Ni or Co into the VO_x-NT vanishes the vibrations at ≈2850, 2920 and 2960 cm^{-1} of the dodecylamine, confirming the successful replacement of the cations for the metals in the solid structure. Moreover, the band at ≈3390 cm^{-1}, which indicates the deformation of O—H groups, remains in both spectra of the $NiVO_x$-NT and $CoVO_x$-NT samples and suggests that the water molecule is included on the layers [26]. Also, the bands assigned to be from V—O bonds broaden, as observed in the low wavenumber region. These results further demonstrate that a slight lattice distortion and microscopic stress variation within the VO_x layers may occur, in a good agreement with the structural disorders detected by the XRD measurements. In case of the $PtVO_x$-NT sample, some bands associated with the dodecylammonium cations bands are not suppressed from the spectra after the Pt impregnation. It seems that the Pt was incorporated mainly on the solid surface with some Pt species on the inner tubes, in line with XRD and TEM results. Besides, the structural disorder of the $PtVO_x$-NT caused by the Pt impregnation suggests that a strong interaction of Pt species with dodecylammonium cation and VO_x occurs.

Micro-Raman spectra of the solids are shown in Fig. 4d. The pristine VO_x-NT has modes located at low frequencies region from 100 to 1000 cm^{-1}. The broad modes at around 171 and 240 cm^{-1} are typical of the V—O bonds from VO_x species [27,28]. The mode at 334 cm^{-1} is more readily assigned to the bending modes of the VO_4 units such as VO_x, in accordance with the literature [28]. At 436–472 cm^{-1}, the out-of-plane bending mode is observed whereas the vibrations at 730, 922 and 987 cm^{-1} are assigned to the symmetric and antisymmetric VO_4 vibrations. Moreover, the micro-Raman spectra of the $NiVO_x$-NT and $CoVO_x$-NT samples are similar to that of the pure VO_x-NT with only two distinctions among the modes in low frequencies; peaks at 286 and 374 cm^{-1}, which suggest the stability of the structure even after ion exchange process. On the contrary, $PtVO_x$-NT has the modes at 730, 922 and 987 cm^{-1} slightly shifted for lower frequencies values than the other samples, an indicative of the Pt strong interaction between with dodecylammonium and VO_x species, as suggested by the FTIR results. Another explanation is that Pt may be marginally affecting the VO_x-NT structure.

At higher frequencies region, the pure VO_x-NT spectrum exhibits broad modes at ≈1150 and ≈1550 cm^{-1} assigned to the vibrations of the docecylamonium cation. These bands have their intensity decreased in $NiVO_x$-NT and $CoVO_x$-NT samples, confirming the structure agent removal of these solids in opposite to that observed for $PtVO_x$-NT, which displays the modes of the dodecylammonium. This is a consequence of the abovementioned interaction of Pt with the VO_x species, as in case of $PtVO_x$-NT. On account of the modes overlapping, no modes from metal oxide vibrations are observed in the metals-containing VO_x-NT samples.

3.2. Textural properties

The textural properties of the solids were investigated through the nitrogen adsorption-desorption isotherms (not shown). All the curves display the type II isotherm, indicating the existence of a steep rise at a low relative pressure. Such a feature is typical of solids possessing a

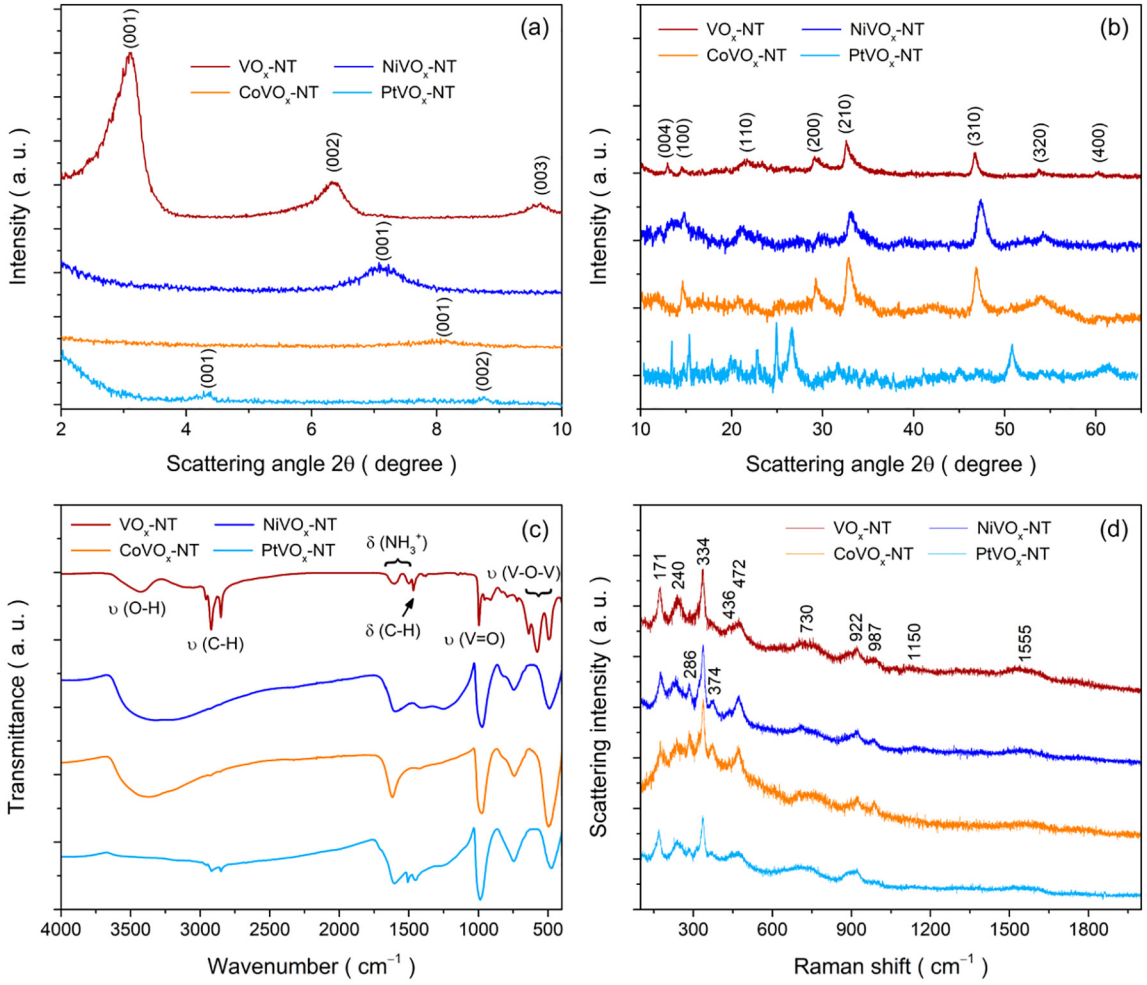

Fig. 4. XRD patterns of metals-containing vanadium oxides nanotubes ($MeVO_x$-NT in which, Me = Ni, Co, and Pt) at (a) low and (b) high diffraction angles. (c) FTIR and (d) micro-Raman spectra.

Table 1
Textural properties of the VO_x NT and $MeVO_x$ NT samples.

Catalyst	BET surface area ($m^2 \cdot g^{-1}$)	*t*-Plot ($m^2 \cdot g^{-1}$)	Pore volume ($cm^3 \cdot g^{-1}$)	Pore size (nm)
VO_x NT	85	3	0.65	8.2
$NiVO_x$ NT	92	5	0.71	9.7
$CoVO_x$ NT	95	5	0.73	13.7
$PtVO_x$ NT	102	6	0.79	15.8

large number of micropores in the interwalls region of the nanotubes, in line with the findings [29,30]. Interestingly, adsorption in the P/P_0 range from 0.2 to 0.8 reveals little mesoporosity. However, the $PtVO_x$-NT is an exception sample, being classified as a type IV curve, according to IUPAC classification. The sample depicts a hysteresis loop between H_3 and H_4 with an indistinct capillary condensation, which is a common feature of mesoporous structure. Besides, an increase in adsorption at a low relative pressure is attributable to the presence of micropores or a strong adsorbate-adsorbent interaction.

Based on the TEM results, the mesoporous structures are associated with the large diameter of the tubes. Furthermore, the intercalation of transition metal species on the VO_x-NTs may form partially damaged nanotubes and the latter having numerous defects, distortions and loops along the tube walls. Consequently, the microporous features of the solid may arise from the slight agglomerations of nanotubes and the presence of transition metal species intercalated within the VO_x-NTs, as well. It is worth mentioning that the $MeVO_x$-NTs, in which Me = Ni, Co and Pt, do not exhibit nitrogen desorption at low pressures; consequently, the agglomeration of the tubes gives a structural network of ultramicropores, where nitrogen molecule is trapped. This suggests that the ultramicropores exist in the solids studied, on the basis of literature results for microporous carbons possessing ultramicropores [31]. We observe a broad pore size distribution for all solids, which comprises of meso and micropores, with the latter being predominant. This is reasonable because the micropores of VO_x-NTs are derived from either the nanotubes agglomeration or metal oxide nanoparticle agglomerations, as aforesaid. Besides, the ultramicropores possessing sizes lesser than 1 nm are also observed. The textural parameters of the solids are listed in Table 1.

Notwithstanding the controversies on using BET surface area for reporting surfaces areas of microporous solids, the surface areas are obtained under the same conditions for relative comparison. For instance, VO_x-NT possesses a BET surface area of ca. $85\ m^2 \cdot g^{-1}$ and a mesopore volume of $0.65\ cm^3 \cdot g^{-1}$, which is lower than the other samples containing metals nanoparticles. Considering the close textural properties between $NiVO_x$-NT ($92\ m^2 \cdot g^{-1}$ and $0.71\ cm^3 \cdot g^{-1}$) and $CoVO_x$-NT ($95\ m^2 \cdot g^{-1}$ and $0.73\ cm^3 \cdot g^{-1}$), the ion exchange process on the two materials is successfully achieved. As a result, the Ni and Co nanoparticles are intercalated on the materials, as seen by SEM analyses. On the contrary, $PtVO_x$-NT has the highest surface area among all solids studied, which indicate the Pt particles are dispersed on the external surface of nanotubes or even intercalated.

Concerning the micropores areas (*t*-plot), the values systematically increased from 3 to $6\ m^2 \cdot g^{-1}$ as the incorporation of the metals occurs.

Table 2
Conversion of glycerol in distinct temperatures in the acetalization of glycerol. The selectivities to the products are taken at 50 °C. The acetalization of glycerol with acetone is carried out with 130 mg of catalyst at 50 °C and glycerol to acetone molar ratio of 1 in 6 h of reaction.

Catalyst	%Glycerol conversion Temperature (°C)			%Selectivity at 50 °C			TOF (h^{-1})	%Metal content[b]
	50	80	110	Solketal	Acetal	Others[a]		
VO_x NT	69.2	37.2	73.0	17.0	1.4	81.6	37	–
$NiVO_x$ NT	67.1	63.4	12.0	22.0	1.9	76.1	36	0.9
$CoVO_x$ NT	50.4	–	–	24.5	2.0	73.5	27	0.5
$PtVO_x$ NT	54.3	–	–	19.8	1.6	78.6	29	0.4

[a] Others can be 2-(hydroxypropan-2-yloxy)propane-1,2-diol, 1,2,3-propanetriol monoacetate, 2,2-dimethyl-[1,3]-diozane-4-il-methanol,3-(2-hydroxypropan-2-yloxy)propane-1,2-diol and byproducts of condensation.
[b] After the catalyst test.

$PtVO_x$-NT has the largest value among the solid studied. This is a clear sign of the Pt effect on the generation of additional porosity to the solid. The average pore size of the VO_x-NT sample is estimated to be 8.2 nm, which is much smaller than the corresponding pore size of $MeVO_x$-NT values. The $PtVO_x$-NT sample has only one distinct peak at about 15.8 nm, suggesting a more uniform mesopore structure due to Pt nanoparticles inside the interwall region, whereas the ones in the 0.5–1.3 nm may arise from the micro and ultramicropores generated by the Pt presence on surface leading to a reduction of random mesopores.

3.3. Acetalization reaction of glycerol with acetone

3.3.1. Temperature effects

The glycerol acetalization with acetone was studied under mild conditions and distinct conditions of temperature and acetone to glycerol molar ratio of 1:1 for 6 h of reaction. The conditions with the corresponding results are shown in Table 2. Depending on the temperature studied, the nanotubes are active in the reaction. At 50 °C, VO_x-NT and $NiVO_x$-NT have comparable glycerol conversions (more than 67%) while the conversions over $CoVO_x$-NT and $PtVO_x$-NT are a little lower but still high, in comparison with other vanadium-containing catalysts [32]. The activity is essentially due to the VO_x species contributions playing a role as acid-base and active redox sites for the reaction. The observed differences in terms of conversions under isothermal conditions are attributed to the stability of VO_x-NT and $NiVO_x$-NT structure through their pore structure with tailorable interlamellar spacing for reaction occurrence. Accordingly, the TOF values of VO_x-NT and $NiVO_x$-NT tested at 50 °C are 37 and 36 h^{-1}, respectively. It is remarkable that these values are far comparable to that of $CoVO_x$-NT and $PtVO_x$-NT. It can be observed that both $CoVO_x$-NT and $PtVO_x$-NT retain a noticeable microporosity leading to the reaction occurrence on their surface where the formation of the voluminous product may impede the process. In addition, the leaching of the Co and Pt species during the reaction is likely as their contents decreased from 1.0 to 0.5 and 0.4 wt % (Table 2), respectively for $CoVO_x$-NT and $PtVO_x$-NT tested at 50 °C. Thereby, the relatively low catalytic performance of these solids is experienced at 50 °C.

Further spent catalysts characterizations demonstrate these assumptions. The AG reaction mainly produces the solketal (five-membered ring ketal) and the acetal (six-membered ring acetal), whose relative formation depends on the acetalization position within the glycerol molecule [12,31]. In all cases, solketal is formed with selectivity in the 17–24% range for all solids at 50 °C, being acetal produced in a lesser amount. The findings state that the glycerol acetalization with acetone gives the formation of the five-membered ring transition state to form solketal [31]. Therefore, the solketal compound possesses the methyl group in axial position and thereby, a steric repulsion may take place being the solketal mainly formed instead of acetal. However, when the reaction temperature is raised to 80 °C (Table 2), only VO_x-NT and $NiVO_x$-NT are actives, whereas the other two samples do not exceed 1% of conversion. Indeed, the glycerol conversion drops dramatically over VO_x-NTs to 37% while $NiVO_x$-NT maintains the stable performance at around 63%. Neither solketal nor acetal is observed at temperatures superior to 80 °C with the prevalence of the byproducts, namely others.

At 110 °C, conversion over NiVOx NT is of ca. 12% after 6 h of reaction. This suggests that the stability of the micro–mesoporous structures is affected by the temperature, which cause change in the reaction mechanism. On the contrary, VOx NT conversion rises to 73% without formation of the main products. It is noteworthy that limited contact among volatile acetone, glycerol and the catalysts can influence in the conversion levels of these solids at high temperatures. Latter observations indicated that, only negligible deactivation of the NiVOx NT catalyst has occurred at lower temperatures than 110 °C for 120 h of the reaction whereas VOx NT was inactive.

The selectivities also greatly decreased at high temperatures with the others major byproducts including 1,2,3-propanetriol monoacetate and 2,2-dimethyl-1,3-dioxolane-4-methanol acetate being formed, instead of the desired solketal and acetal. These results are actually expected once the literature reports showed that exothermic reactions led to high temperatures result in lower equilibrium product yield [2].

3.3.2. Effect of the catalyst amount

The glycerol acetalization with acetone was also performed with different catalyst amounts at 50 °C and acetone to glycerol molar ratio of 1:1 over the VO_x-NT and $NiVO_x$-NT samples. The results are exhibited in Fig. 5a. As can be observed, the reaction proceeds with a low conversion, when the reduced amounts of ca. 65 mg solids are used in the reaction. However, on this condition, the $NiVO_x$-NT catalyst is more active than VO_x-NT due to the Ni^{2+} species (XPS results) in the former sample acting concomitantly with VO_x sites, as stated before. Nevertheless, when the amount of catalyst is increased to 130 mg, the conversion greatly raised to nearly 65%, irrespective of the catalysts used. A primary reason for similar performances is the surface availability of a total number of VO_x active sites in both solids assisting to the glycerol acetalization with acetone.

Conducting the reaction with an amount higher than 130 mg it is expected that no significant effect on the yield occurs [5,12]. However, the impact of increasing the catalyst amounts for 260 mg provide benefits in terms of conversions of glycerol with $NiVO_x$-NT exhibiting the best catalytic performance. In all cases, the solketal selectivity is too low due to the parallel reaction involving the glycerol, acetone and the products formed at high catalyst loadings. As reported in the literature, the compound solketal is thermodynamically more stable than acetal [33], independently on the catalyst amount used.

Hence, the catalysts display a high performance with a maximum conversion of 65% using 130 mg of solid.

3.3.3. Acetone to glycerol molar ratios

The effects of the acetone to glycerol molar ratios on the conversion

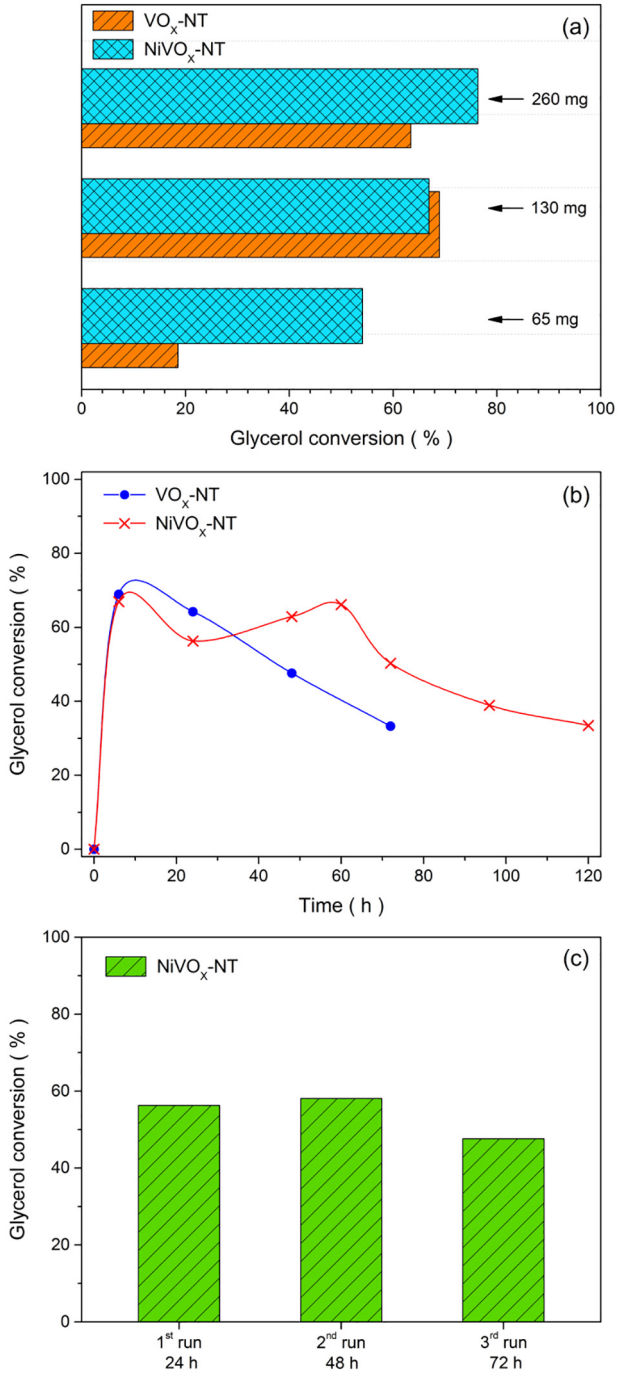

Fig. 5. (a) Effect of the catalyst amount in the acetalization of glycerol with acetone. (b) Evaluation of the glycerol conversion versus reaction time. (c) Catalyst recyclability along of several runs of 24 lh. In all cases, reaction conditions are a temperature of 50 °C and acetone to glycerol molar ratio of 1:1.

Table 3
Conversion of glycerol and selectivity to the products by varying the glycerol to acetone molar ratios. The acetalization of glycerol with acetone is carried out with 130 mg of catalyst at 50 °C.

Catalyst	%Glycerol conversion Acetone to glycerol molar ratio			%Selectivity to solketal Acetone to glycerol molar ratio		
	1:1	1:4	1:8	1:1	1:4	1:8
VO_x NT	69.2	43.9	76.2	36.8	17.0	46.2
$NiVO_x$ NT	67.1	59.2	50.8	24.8	22.0	53.2

and selectivity were investigated. With regard to AG reaction at acetone to glycerol molar ratio of 1:1, all catalysts are actives with VO_x-NT and $NiVO_x$-NT having the best performances (Table 2). As acetone to glycerol molar ratios is distinct from 1:1, deleterious effect on the catalytic parameters of $CoVO_x$-NT and $PtVO_x$-NT are experienced. This is due to the Co and Pt affinities by acetone in condensation reactions producing byproducts, without the occurrence of the acetylation of glycerol [34,35]. Therefore, a performance comparison of the most active acetalization catalysts, viz. VO_x-NT and $NiVO_x$-NT are explored at 50 °C with a catalyst mass of 130 mg for 6 h of reaction. The results are summarized in the Table 3.

It is seen that upon increasing the acetone to glycerol molar ratio from 1:1 to 4:1 the conversion falls in both VO_x-NT and $NiVO_x$-NT catalysts. For instance, glycerol conversion over $NiVO_x$-NT decays from 67.1 (acetone to glycerol molar ratio to 1:1) to 59.2% (acetone to glycerol molar ratio to 4:1). It is known that acetone concentrations are the limiting factor to favor the forward reaction of glycerol acetalization, in opposite to high amount of glycerol speeding up the conversions [5]. This effect is more significant for pure VO_x-NT, most likely due to the deactivation of the latter by structural changes, as later shown by TEM analysis.

Indeed, it is found that the selectivities to the products depend on the acetone to glycerol molar ratios. When the ratio is 1:4, the solketal production drops from 24.8 to 22.0% over $NiVO_x$ NT with similar effects for VO_x NT. Further increasing of the acetone to glycerol molar ratio to ratio is 1:8 over $NiVO_x$ NT led to a much high solketal selectivity of 53.2% with a little fraction of acetone condensation byproducts. On the contrary, selectivity to solketal increases greatly from 17.0 to 46.2% over VO_x NT with a concurrent decrease in the selectivity for byproducts at a acetone to glycerol molar ratio to ratio is 1:8. Additionally, the presence of an excess of acetone has a dual effect in both increasing the selectivity to the solketal in addition to inhibiting the conversion. These results agree well with the performances in glycerol acetalization carried out using other catalysts under the same conditions [5,12].

Hence, the further investigations were conducted at acetone to glycerol molar ratio of 1:1, as an optimum balance between conversion and selectivity to the main products. The spent solids characterization shown in what follows will reveal that these catalysts have resistance against deactivation by phase transformation and leaching of VO_x and NiO actives sites, as well.

3.3.4. Evaluation of the glycerol conversion versus reaction time and catalyst recyclability

The conversion is evaluated as a function of time for acetone to glycerol molar ratio of 1:1 at 50 °C and using 130 mg of solid (Fig. 5b).

At the beginning of the reaction, the catalysts have very similar behavior with a conversion of glycerol of ca. 70%, which is indeed close to the equilibrium conditions, in accordance with the literature results [31,32,36]. As the reaction proceeds, the acetalization reaction proceeds faster over $NiVO_x$ NT than VO_x NT. Over the course of the reaction, VO_x NT experiences a decay in terms of conversion whereas $NiVO_x$ NT reaches a plateau at longer reaction times till 80 h of reaction. At 120 h of reaction, VO_x NT completely deactivates while $NiVO_x$ NT has a slight drop in its performance, achieving 40% of glycerol conversion. This result can be understood in terms of the presence of Ni^{2+} included in the VO_x sites, as illustrated by XPS and XRD.

The catalyst recyclability of the solids was also investigated in order to determine their stabilities towards three repeated reactions of 24 h, under the same conditions. The reuses of the catalysts consisted of testing the solids under the optimal reaction conditions at 50 °C, catalyst mass of 130 mg with acetone to glycerol molar ratio of 1:1. Briefly, the mixture was allowed to react for 24 h for each run with the subsequent centrifugation of the solid. The catalyst was then washed, dried and again reused in runs at regular 24 h intervals [12]. The reaction progress was monitored by GC and the liquid filtrated was analyzed.

Preliminary, a blank experiment was first performed in the presence of dodecylamine and it was observed that no homogeneous reaction has occurred.

The recycling experiments were performed over the most active catalysts, i.e., VO_x-NT and $NiVO_x$-NT after being used for the first time in 24 h. However, the VO_x-NT completely deactivated in the first recycle. In the 1st run, the glycerol conversion of the VO_x-NT and $NiVO_x$-NT samples were 0.2 and 55% (with a low amount of solketal and acetal production) and the TOF values being 0.16 and 29 h^{-1}, respectively. Fig. 5c shows only the recyclability of the $NiVO_x$-NT sample along of three runs of 24 h. A liquid filtrate analysis of the $NiVO_x$-NT sample after the recycling experiment accounts for 0.9 wt% of Ni, indicating that the metal content remains almost unchanged, as its total content the filtrate is l.0 wt%.

A slight increase in glycerol conversion is observed for $NiVO_x$-NT in the 2nd use with the same trends for the TOF. This could be attributed to the inevitable loss of nickel species in the second repeated reaction, as further seen by spent catalysts characterizations. It is worthwhile to note that the catalytic parameters of $NiVO_x$-NT slightly decreased in the third use with 50% of glycerol conversion. This indicates the loss of the nanoparticles with the subsequent decrease of the superficial area gives a slight decrease in the catalytic activity. Moreover, the catalytic reaction efficiency for the desired products over $NiVO_x$-NT including solketal is low with the byproducts predominance of about 50%.

As some catalyst losses may occur during the third step, we added an amount of fresh catalyst about, being 4% of the total weight, which is similar to other procedure using the reusable catalyst in the literature [12]. In spite of enhancing the catalytic performance, the glycerol conversion drops to 10% with a TOF of 5 h^{-1} in the 4th use while the solketal selectivity is only 1%. Again, the byproducts selectivity is preferred in the fourth use. At this stage, the physical degradation of the $NiVO_x$-NT seems to be the leading cause of the deactivation. Unlike VO_x-NT, the recycle number of $NiVO_x$-NT is restricted to 3 cycles as consequence of degradation during the reaction cycles.

The $NiVO_x$-NT catalyst in study shows advantages over other V-based samples present in the literature [14,32] due to the high glycerol conversions and stability achieved by adding Ni to the VO_x-NT nanotubes.

3.3.5. Reaction with different substrates

Following the results obtained with $NiVO_x$-NT, the substrate screening was then extended to three other aldehydes, namely furfuraldehyde, benzaldehyde and butyraldehyde in order to investigate the influence of these substrates on the glycerol conversion to solketal and acetal production. The glycerol conversion and selectivities values are summarized in Table 4. The results demonstrate that all substrates are reactive with glycerol, except the furfuraldehyde. In addition, the glycerol conversion reaches values superior to 24% with using butyraldehyde and benzaldehyde in 6 h of reaction, being the $NiVO_x$-NT catalyst highly selective for “others”. Because the butyraldehyde is a linear aldehyde, one can take full advantage of its carbonyl available for reaction with alcohols to efficiently obtain the conversion of glycerol with desired cycle's products formation [37]. Consistent with these results, the butyraldehyde self-reaction may occur to produce 2-ethyl-2-hexenal [38]. Therefore, can be proposed that butyraldehyde acts reacting in self-parallel reactions, as it clearly favored linear molecules formation over the cycle ones.

Table 4
Conversion of glycerol and selectivity to the products with distinct substrates over $NiVO_x$ NT. Values in parenthesis represents the substrate conversion. The acetalization of glycerol with substrate is carried out with 130 mg of catalyst at 50 °C and acetone to glycerol molar ratio of 1.

Substrate	Conversion (%)		Selectivity (%)	
	Solketal		Acetal	Others
BUT	24.0 (16)	51.0	1.7	47.3
FUR	0.2 (20)	27.1	5.0	67.9
BEN	28.0 (0)	35.0	1.1	63.9
Acetone	67.1 (15)	22.0	1.9	76.1

Concerning the substrate conversion, furfuraldehyde itself has the remarkable conversion observed during this screening of ca. 20% followed by butyraldehyde whereas the benzaldehyde conversion is inactive in the reaction. For the benzaldehyde, the steric hindrance of the voluminous molecule can impede the attack of the activated carbonyl group to glycerol. As a result, this prevents excessive self-reactions giving a low reactivity towards glycerol. Moreover, furfuraldehyde and, to a lesser extent, butyraldehyde are active for the hemiketal intermediate formation, thus favoring the formation of the cyclic molecules. Meanwhile, parallel reactions such as 2-ethyl-2-hexenal (aldol condensation) and self-furfuraldehyde condensation are significant [38,39], since selectivity values of solketal production remain lesser than 51%, irrespective of the aldehyde used.

Except for the butyraldehyde as a substrate, large amounts of others products are noticed, dissimilar to the previously tested acetone compound. Judging from these results, the impact of the use of aldehyde or ketone on the selectivity of the reaction appears to be relevant. Along with the influence of the substrate that arises from its reactivity reaction, one should consider the glycerol alcohol, of which all three hydroxyls are differentiated by reactivity.

It is suggested that the carbonyl group may play an important role of a greater labiality of the aldehyde than that of the ketones towards the VO_x and Ni^{2+} sites. Literature reports show that the activation of the carbonyl compound by the catalysts is the main step of the reaction to form the hemiacetal or ketal intermediates [31] and thereby, the aldehydes modulating the catalytic activity of the $NiVO_x$-NT. Hence, the VO_x active sites are much less likely to severely deactivated by the ketone, in which the retro-aldol parallel reactions are not favored, thus allowing high selectivities to solketal and acetal to be achieved, depending on the acetalization reaction condition used. Therefore, the strong role played by the catalyst properties in tuning the balance between structural and textural properties may lead to more stability of the solids and attainable solketal pool products.

3.4. Catalysts used after the reaction

3.4.1. TEM analysis

The TEM observations of the spent $NiVO_x$-NT tested with the different substrates are shown in Fig. 6. TEM image of the catalyst tested with furfuraldehyde, Fig. 6a and b clearly demonstrate that the NiO nanoparticles remain in the solid through the lattice spacing of ca. 0.205 nm that can be indexed to the (111) plane. On the contrary, the nanotubes did not exhibit such a stable structure as that of the Fig. 3b in the presence of furfuraldehyde. Indeed, some of the tubes collapsed forming opened structures and residual amorphous carbon. Although the lack of the tubular morphology was unfavorable for AG reaction occurrence, the furfuraldehyde conversion is observed due to its affinity for nickel [40]. When the $NiVO_x$-NT is tested in the presence of butyraldehyde (Fig. 6c) and benzaldehyde (Fig. 6d) a similar morphology is seen. In contrast, the Ni nanoparticles are evenly distributed over the opened $NiVO_x$-NT nanotubes, most probably in reason of some leaching nanoparticles during the reaction. In this case, the little Ni particles are favorable to the AG reaction occurrence, as depicted in Table 3. Thereby, TEM results of $NiVO_x$-NT tested using distinct substrates show that the nanotubes shape has changed and the sizes of the Ni particles got smaller.

3.4.2. Surface oxidation state of the spent $NiVO_x$-NT tested with different substrates

The oxidation states of the elements on the solid surface, i.e., the spent $NiVO_x$-NT tested with the different substrates (aldehydes), were

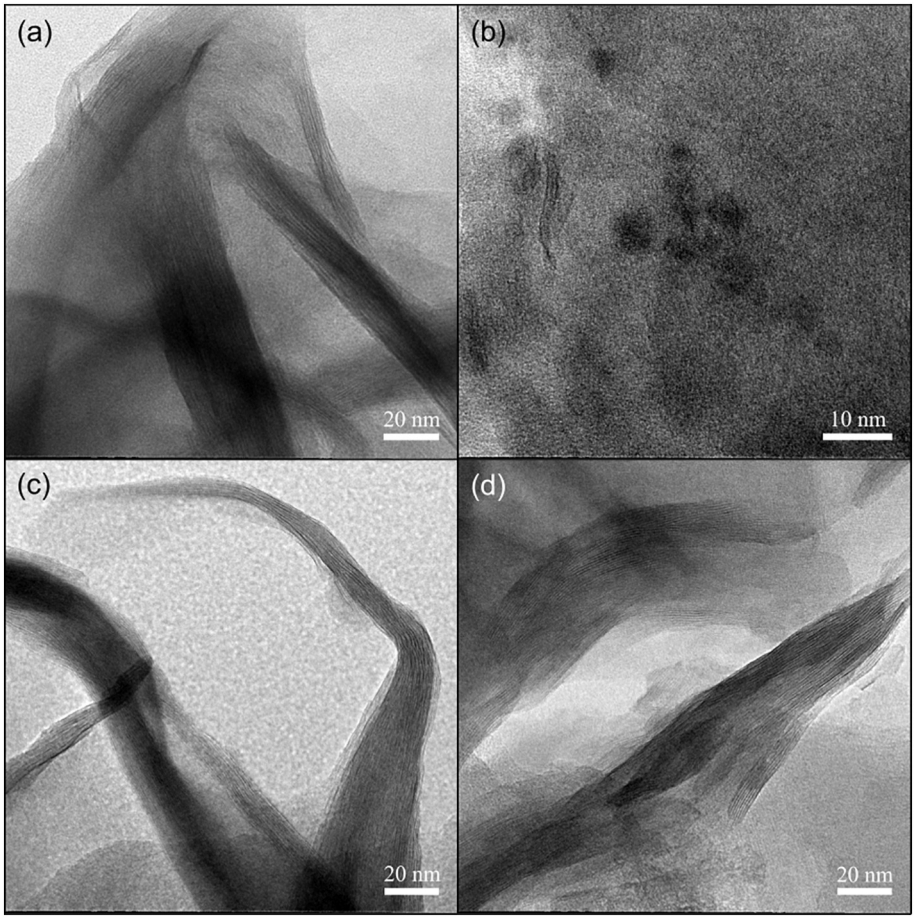

Fig. 6. TEM images of the $NiVO_x$-NT tested with different substrates: (a) furfuraldehyde, (b) furfuraldehyde in a higher magnification, (c) butyraldehyde, and (d) benzaldehyde. Reaction conditions: temperature of 50 °C and substrate to glycerol molar ratio of 1:1 for 6 h of reaction.

Table 5
XPS data of the spent $NiVO_x$ NTs nanotubes.

Sample and substrate used	Ni 2*p*	V 2*p*	C 1*s*	N*1s*	O 1*s*
$NiVO_x$ NT	–	516.1	284.8	401.4	530.1
FUR		517.3	286.2		531.9
			287.2		533.1
			288.6		
$NiVO_x$ NT	856.5	516.1			530.0
BEN		517.3	284.8		531.7
			286.1		533.1
$NiVO_x$ NT			286.8		
BUT			288.6		
		516.0		–	
	856.6	517.2			529.8
		515.7	284.7		531.8
			285.9		533.0
			287.3		
			288.7		
				401.2	

The accuracy on the BE values is of ca. ± 0.1 eV.

inferred through XPS measurements. The assignments are summarized in Table 5. The catalyst tested with the furfuraldehyde has V 2*p* core levels comprising V $2p_{3/2}$ and V $2p_{1/2}$ peaks (not shown). The broad V $2p_{3/2}$ peak can be perfectly deconvoluted into two peaks with binding energies (BE) at around 516.1 and 517.3 eV, which are attributed to the V^{4+} and V^{5+}, respectively [26,41]. It is noted that the V 2*p* core level is unchanged for all samples. However, the $NiVO_x$-NT tested with butyraldehyde has an extra BE at around 515.7 eV, which suggest the presence of V^{3+} in concomitance to those of V^{5+} and V^{4+}. This observation agrees with the earlier finding that the V exists in a partially reduced state as VO_x species [41]. The O 1*s* core level spectra have three components centered at about 530.1, 532.9 and 533.1 eV for all samples. These BE are ascribed to contributions from the O—V—O and from the defective oxides components inherent in the V_2O_5, VO_2 and V_2O_3 in several oxidation states [26,42,43], named herein as VO_x entities. Such a feature is independent of the substrate tested. Moreover, the N 1*s* level from the dodecylamine is found at about 401.2 ± 0.1 eV, corroborating with the data found elsewhere [44]. Importantly, the N 1*s* from dodecylamine is solely found over $NiVO_x$-NT tested with butyraldehyde and furfuraldehyde. This evidences that the structuring agent vanishes from the solid tested with benzaldehyde. It can also suggest the lack of reactivity of the benzaldehyde substrate towards glycerol (Table 4).

The contributions of the C 1*s* core level (Fig. 7) come from the alkyl groups of the structuring agent, as observed through the BE at ≈285 eV (aliphatic C—C and aromatic C═C groups) and at ≈286 eV (C—N) and consistent with the literature reports [44]. Moreover, the carbonyl carbon C═O form the aldehydes at ≈287 eV are observed concomitantly with that of carboxylate carbon C—O—C groups at ≈289 eV [44,45]. Also, there is no distinction in the XPS spectra of the various substrates concerning the kind of carbon deposition on the solid surface. The Ni 2*p* core-level spectrum shows a Ni $2p_{3/2}$ main peak centered at ≈856.5 eV, typically of Ni^{2+} [45]. This contribution is also observed when the sample is tested with butyraldehyde and benzaldehyde. When the substrate is furfuraldehyde, there was no detection of Ni 2*p* signal.

The AG reaction over the vanadate nanotubes may occur over a mechanism that the VO_x species works as Lewis acid metal sites in the

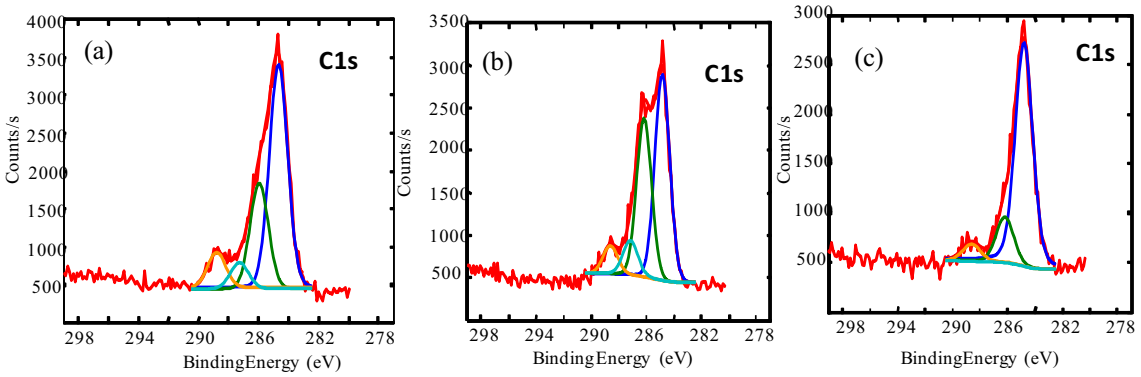

Fig. 7. XPS spectra of C *1s* core level of spent NiVOx NT tested with the following substrates: (a) buthyraldehyde, (b) furfuraldehyde and (d) benzaldehyde.

ketalization reaction to activate the acetone carbonyl group through coordination to acetone by activating its carbonyl group, as found elsewhere for catalyst-containing Lewis acid metal sites [31,46–48]. Then, the activated carbonyl species are attacked by the nucleophilic hydroxyl group of glycerol, accompanied by the formation of a bond between the carbonyl oxygen atom and the β-carbon of the glycerol and by dehydration, resulting in the formation of the intermediate hemiacetal compound. Subsequently, there is a water elimination step to the formation of solketal [46,47].

Simultaneously, a redox cycle between V^{5+}/V^{4+} would promote the collapse of the tube structure leading to develop opened nanotubes and Ni nanoparticles. Accordingly, the Ni^{2+} ions are mostly from the structure within the VO_x layers, when the tubular structure changes without affecting the AG reaction. In the case of the VO_x-NT, the structuring agent is absent after the reaction by collapsing the tubes and decreasing the catalytic performance at certain reaction conditions. However, intercalating the VO_x-NTs with Ni one can change the morphology and suppress a phase transformation, resulting in a much better Ni dispersion than the other catalysts. Moreover, a variation of the reaction conditions and recycling the catalyst did not cause the evolution of the tubes to nanoplates, indicating that NiO nanoparticles are finely dispersed on the support.

4. Conclusions

The vanadium oxide nanotubes (VO_x-NTs) containing metals were successfully prepared. Depending on the extent of involvement of the metal site, such as Ni, Co, or Pt, the materials were highly actives in the acetalization of glycerol. The effects of the temperature, catalysts mass and acetone to glycerol molar ratio conditions were evaluated. The catalysts activities were in accordance with their redox, structural and textural properties. The Co and Pt-based solids were deactivated during the AG reaction, due to their lack of stability. In contrast, the pure VO_x-NT and $NiVO_x$-NT catalysts gave best results in the reaction due to either VO_x and Ni^{2+} active sites presence or a combination of them. Comparing the ketone with the used aldehydes as substrates for the reaction, the acetone proved to be the best substrate to be used giving high solketal selectivity.

Acknowledgments

The CNPq (470793/2013-9) and FUNCAP (23038.008860/2013-92) are acknowledged for funding this research. DCC is recipient of the CAPES Ph.D. scholarship. Thanks to Samuel Tehuacanero Núñez, and Dr. Jesús Arenas-Alatorre from LCM IFUNAM for the comments and support in the TEM images. ERC thanks to the project CTQ2015-68951-C3-3-R (Ministerio de Economía y Competitividad, Spain) and FEDER funds. We would like to thank CETENE-INT and Central Analítica da UFC for performing some characterizations of the materials.

References

[1] H.W. Tan, A.R. Abdul Aziz, M.K. Aroua, Glycerol production and its applications as a raw material: a review, Renew. Sust. Energ. Rev. 27 (2013) 118–127.
[2] X. Hu, R. Gunawan, D. Mourant, M.D. Mahmudul Hasan, L. Wu, Y. Song, C. Lievens, Chun-Zhu Li, Upgrading of bio-oil via acid-catalyzed reactions in alcohols — a mini review, Fuel Process. Technol. 155 (2017) 2–19.
[3] D.C. Carvalho, A.C. Oliveira, O.P. Ferreira, J.M. Filho, S. Tehuacanero-Cuapa, A.C. Oliveira, Titanate nanotubes as acid catalysts for acetalization of glycerol with acetone: influence of the synthesis time and the role of structure on the catalytic performance, Chem. Eng. J. 313 (2017) 1454–1467.
[4] I. Agirre, M.B. Güemez, A. Ugarte, J. Requies, V.L. Barrio, J.F. Cambra, P.L. Arias, Glycerol acetals as diesel additives: kinetic study of the reaction between glycerol and acetaldehyde, Fuel Process. Technol. 116 (2013) 182–188.
[5] W. Qing, J. Chen, X. Shi, J. Wu, J. Hu, W. Zhang, Conversion enhancement for acetalization using a catalytically active membrane in a pervaporation membrane reactor, Chem. Eng. J. 313 (2017) 1396–1405.
[6] A. Namdeo, S.M. Mahajani, A.K. Suresh, Palladium catalysed oxidation of glycerol—Effect of catalyst support, J. Mol. Catal. A Chem. 421 (2016) 45–56.
[7] A. Carrero, J.A. Calles, L. García-Moreno, A.J. Vizcaíno, Production of renewable hydrogen from glycerol steam reforming over bimetallic Ni-(Cu,Co,Cr) catalysts supported on SBA-15 silica, Catalysts 7 (2017) 55.
[8] F.A.A. Barros, H.S.A. de Sousa, A.C. Oliveira, M.C. Junior, J.M. Filho, B.C. Viana, A.C. Oliveira, Characterisation of high surface area nanocomposites for glycerol transformation: effect of the presence of silica on the structure and catalytic activity, Catal. Today 212 (2013) 127–136.
[9] P. Sudarsanam, B. Mallesham, A.N. Prasad, P.S. Reddy, B.M. Reddy, Synthesis of bio–additive fuels from acetalization of glycerol with benzaldehyde over molybdenum promoted green solid acid catalysts, Fuel Process. Technol. 106 (2013) 539–545.
[10] M. Shirani, H.S. Ghaziaska, C. Xu, Optimization of glycerol ketalization to produce solketal as biodiesel additive in a continuous reactor with subcritical acetone using Purolite® PD206 as catalyst, Fuel Process. Technol. 124 (2014) 206–211.
[11] L. Chen, B. Nohair, D. Zhao, S. Kaliaguine, Glycerol acetalization with formaldehyde using heteropolyacid salts supported on mesostructured silica, Appl. Catal. A Gen. 549 (2018) 207–215.
[12] I.S. Gomes, D.C. de Carvalho, A.C. Oliveira, E. Rodríguez-Castellón, S. Tehuacanero-Cuapa, P.T.C. Freire, J.M. Filho, G.D. Saraiva, F.F. Sousa, R. Lang, On the reasons for deactivation of titanate nanotubes with metals catalysts in the acetalization of glycerol with acetone, Chem. Eng. J. 334 (2018) 1927–1942.
[13] L.J. Konwar, A. Samikannu, P.M. Arvela, D. Boström, J.-P. Mikkola, Lignosulfonate-based macro/mesoporous solid protonic acids for acetalization of glycerol to bio-additives, Appl. Catal. B Environ. 220 (2018) 314–323.
[14] T.E. Souza, M.F. Portilho, P.M.T.G. Souza, P.P. Souza, L.C.A. Oliveira, Modified niobium oxyhydroxide catalyst: an acetalization reaction to produce bio-additives for sustainable use of waste glycerol, ChemCatChem 6 (2014) 2961–2969.
[15] C. Ferreira, A. Araujo, V. Calvino-Casilda, M.G. Cutrufello, E. Rombi, A.M. Fonseca, M.A. Bañares, I.C. Neves, Y zeolite-supported niobium pentoxide catalysts for the glycerol acetalization reaction, Microporous Mesoporous Mater. 271 (2018) 243–251.
[16] B.L. Wegenhart, S. Liu, M. Thom, D. Stanley, M.M. Abu-Omar, Solvent-free methods for making acetals derived from glycerol and furfural and their use as a biodiesel fuel component, ACS Catal. 2 (2012) 2524–2530.
[17] B. Mallesham, P. Sudarsanam, G. Raju, B.M. Reddy, Design of highly efficient Mo and W-promoted SnO_2 solid acids for heterogeneous catalysis: acetalization of bio-glycerol, Green Chem. 15 (2013) 478–489.
[18] M. Niederberger, H.J. Muhr, F. Krumeich, F. Bieri, D. Gunther, R. Nesper, Low-cost synthesis of vanadium oxide nanotubes via two novel non-alkoxide routes, Chem. Mater. 1 (2000) 1995.
[19] K.-F. Zhang, D.-J. Guo, X. Liu, J. Li, H.-L. Li, Z.-X. Su, Vanadium oxide nanotubes as the support of Pd catalysts for methanol oxidation in alkaline solution, J. Power Sources 162 (2006) 1077–1081.
[20] A.C. Santulli, W. Xu, J.B. Parise, L. Wu, M.C. Aronson, F. Zhang, C.-Y. Nam, C.T. Black, A.L. Tiano, S.S. Wong, Synthesis and characterization of V_2O_3 nanorods,

Phys. Chem. Chem. Phys. 11 (2009) 3718–3726.
[21] L.I. Vera-Robles, A. Campero, A novel approach to vanadium oxide nanotubes by oxidation of V^{4+} species, J. Phys. Chem. C 112 (2008) 19930–19933.
[22] E.V. Aguiar, L.O.O. Costa, M.A. Fraga, Impregnating ionic Pt species on vanadium oxide nanotubes, Catal. Today 142 (2009) 207–210.
[23] G.S. Zakharova, Y. Liu, A.N. Enyashin, X. Yang, J. Zhou, W. Jin, W. Chen, Metal cations doped vanadium oxide nanotubes: synthesis, electronic structure, and gas sensing properties, Sensors Actuators B Chem. 256 (2018) 1021–1029.
[24] X. Zhou, G. Wu, G. Gao, J. Wang, H. Yang, J. Wu, J. Shen, B. Zhou, Z. Zhang, Electrochemical performance improvement of vanadium oxide nanotubes as cathode materials for lithium ion batteries through ferric ion exchange technique, J. Phys. Chem. C 116 (2012) 21685–21692.
[25] L.Z. Pei, Y.Q. Pei, Y.K. Xie, C.Z. Yuan, D.K. Li, Q.-F. Zhang, Growth of calcium vanadate nanorods, CrystEngComm 14 (2012) 4262–4265.
[26] B. Azambre, M.J. Hudson, O. Heintz, Opotactic redox reactions of copper(II) and iron(III) salts within VO_x nanotubes, J. Mater. Chem. 13 (2003) 385–393.
[27] R.L. Frost, D.A. Henry, M.L. Weier, W. Martens, Raman spectroscopy of three polymorphs of $BiVO_4$: clinobisvanite, dreyerite and pucherite, with comparisons to $(VO_4)^{3-}$-bearing minerals: namibite, pottsite and schumacherite, J. Raman Spectrosc. 37 (2006) 722–732.
[28] F.D. Hardcastle, I.E. Wachs, Determination of vanadium-oxygen bond distances and bond orders by Raman spectroscopy, J. Phys. Chem. 95 (1991) 5031.
[29] M. Fu, C. Ge, Z. Hou, J. Cao, B. He, F. Zeng, Y. Kuang, Graphene/vanadium oxide nanotubes composite as electrode material for electrochemical capacitors, Phys. B Condens. Matter 421 (2013) 77–82.
[30] C. Bai, J. Li, S. Liu, X. Yang, X. Yang, Y. Tian, K. Cao, Y. Huang, L. Ma, S. Li, In situ preparation of nitrogen-rich and functional ultramicroporous carbonaceous COFs by "segregated" microwave irradiation, Microporous Mesoporous Mater. 197 (2014) 148–155.
[31] S. Gadamsetti, N.P. Rajan, G.S. Rao, K.V.R. Chary, Acetalization of glycerol with acetone to bio fuel additives over supported molybdenum phosphate catalysts, J. Mol. Catal. A Chem. 410 (2015) 49–57.
[32] L.H. Vieira, L.G. Possato, T.F. Chaves, S.H. Pulcinelli, C.V. Santilli, L. Martins, Studies on dispersion and reactivity of vanadium oxides deposited on lamellar ferrierite zeolites for condensation of glycerol into bulky products, Mol. Catal. (2017), https://doi.org/10.1016/j.mcat.2017.11.027 (in press).
[33] V. Calvino-Casilda, K. Stawicka, M. Trejda, M. Ziolek, M.A. Bañares, Real-time Raman monitoring and control of the catalytic acetalization of glycerol with acetone over modified mesoporous cellular foams, J. Phys. Chem. C 118 (2014) 10780–10791.
[34] K. Pupovac, R. Palkovits, Cu/MgAl(2)O(4) as bifunctional catalyst for aldol condensation of 5-hydroxymethylfurfural and selective transfer hydrogenation, ChemSusChem 6 (2013) 2103–2110.
[35] S. Herrmann, E. Iglesia, Elementary steps in acetone condensation reactions catalyzed by aluminosilicates with diverse void structures, J. Catal. 346 (2017) 134–153.
[36] R. Rodrigues, D. Mandelli, N.S. Goncalves, P.P. Pescarmona, W.A. Carvalho, Acetalization of acetone with glycerol catalyzed by niobium-aluminum mixed oxides synthesized by a sol–gel process, J. Mol. Catal. A Chem. 422 (2016) 122–130.
[37] M.B. Güemez, J. Requies, I. Agirre, P.L. Arias, V.L. Barrio, J.F. Cambra, Acetalization reaction between glycerol and n-butyraldehyde using an acidic ion exchange resin. Kinetic modelling, Chem. Eng. J. 228 (2013) 300–307.
[38] X. Zhang, H. An, H. Zhang, X. Zhao, Y. Wang, Ind. Eng. Chem. Res. 53 (2014) 16707–16714.
[39] O.O. James, S. Maity, L.A. Usman, K.O. Ajanaku, O.O. Ajani, T.O. Siyanbol, S. Sahu, R. Chaubey, Towards the conversion of carbohydrate biomass feedstocks to biofuels via hydroxylmethylfurfural, Energy Environ. Sci. 3 (2010) 1833–1850.
[40] S.P. Lee, Y.-W. Chen, Selective hydrogenation of furfural on Ni–P, Ni–B, and Ni–P–B ultrafine materials, Ind. Eng. Chem. Res. 38 (1999) 2548–2556.
[41] R. Li, X. Zhu, X. Yan, D. Shou, X. Zhou, W. Chen, Single component gold on protonated titanate nanotubes for surface-charge-mediated, additive-free dehydrogenation of formic acid into hydrogen, RSC Adv. 6 (2016) 100103.
[42] G.S. Wong, J.M. Vohs, An XPS study of the growth and electronic structure of vanadia films supported on CeO_2(111), Surf. Sci. 498 (2002) 266–274.
[43] G. Silversmit, D. Depla, H. Poelman, G.B. Marin, R. De Gryse, An XPS study on the surface reduction of V_2O_5(001) induced by Ar^+ ion bombardment, Surf. Sci. 600 (2006) 3512–3517.
[44] P. Chen, H. Li, S. Song, X. Weng, D. He, Y. Zhao, Adsorption of dodecylamine hydrochloride on graphene oxide in water, Results Phys. 7 (2017) 2281–2288.
[45] D.C. Coelho, A.C. Oliveira, J.M. Filho, A.C. Oliveira, A.F. Lucredio, E.M. Elisabete, E. Rodríguez-Castellón, Effect of the active metal on the catalytic activity of the titanate nanotubes for dry reforming of methane, Chem. Eng. J. 290 (2016) 438–453.
[46] F.D.L. Menezes, M.D.O. Guimaraes, M.J. da Silva, Ind. Eng. Chem. Res. 52 (2013) 16709–16713.
[47] L. Li, T.I. Koranyi, B.F. Sels, P.P. Pescarmona, Green Chem. 14 (2012) 1611–1619.
[48] S.K. Kundu, R. Singuru, T. Hayashi, Y. Hijikata, S. Irle, J. Mondal, Constructing sulfonic acid functionalized anthracene derived conjugated porous organic polymer for efficient metal-free catalytic acetalization of bio-glycerol, ChemistrySelect 2 (2017) 4705–4716.